Nuclear Science and Techniques (2023) 34:5
https://doi.org/10.1007/s41365-022-01159-y

The complex momentum representation approach and its application to low-lying resonances in ^{17}O and ^{29,31}F

Si-Zhe Xu[1] · Shi-Sheng Zhang[1] · Xiao-Qian Jiang[1] · Michael Scott Smith[2]

Received: 12 July 2022 / Revised: 15 November 2022 / Accepted: 18 November 2022 / Published online: 9 January 2023

Abstract
Approaches for predicting low-lying resonances, uniformly treating bound, and resonant levels have been a long-standing goal in nuclear theory. Accordingly, we explored the viability of the complex momentum representation (CMR) approach coupled with new potentials. We focus on predicting the energy of the low-lying $2p_{3/2}$ resonance in ^{17}O, which is critical for s-process nucleosynthesis and missing in previous theoretical research. Using a Woods-Saxon potential based on the Koning-Delaroche optical model and constrained by the experimental one-neutron separation energy, we successfully predicted the resonant energy of this level for the first time. Our predictions of the bound levels and $1d_{3/2}$ resonance agree well with the measurement results. Additionally, we utilize this approach to study the near-threshold resonances that play a role when forming a two-neutron halo in ^{29,31}F. We found that the CMR-based predictions of the bound-level energies and unbound $1f_{7/2}$ level agree well with the results obtained using the scattering phase shift method. Subsequently, we successfully found a solution for the $2p_{3/2}$ resonance with energy just above the threshold, which is decisive for halo formation.

Keywords Neutron capture · Low-lying resonance · Complex momentum representation · Resonance energy

1 Introduction

The weak *s*-process in massive stars [1], driven by neutron capture on heavy isotopes, is thought to be responsible for the synthesis of nuclides in the mass range of 60-90. However, ^{16}O is known to serve as a “neutron poison,” disrupting the weak *s*-process by capturing neutrons that would otherwise be consumed in neutron capture on heavier elements. Variations in the neutron capture rate on ^{16}O have been proven to affect the abundances predicted to be formed in the weak *s*-process [2]. Studies have demonstrated that contributions from low-lying (*i.e.*, near-threshold) ^{17}O resonances make the main contribution to the total neutron capture on ^{16}O at energies beyond 70 keV [3, 4]. The low-lying $1d_{3/2}$ and $2p_{3/2}$ levels in ^{17}O are especially crucial.

Developing the theoretical tools to predict the properties of such low-lying, low angular momentum levels is critical, especially for nucleosynthesis processes relying on neutron capture cross sections of unstable nuclei that have not been measured. The methods that can uniformly treat the bound and resonant levels are particularly important. One theoretical approach, the self-consistent microscopic RAB approach, provides structural information via the analytical continuation of the coupling constant (ACCC) method based on the relativistic mean field (RMF) theory with the Bardeen–Cooper–Schrieffer (BCS) pairing approximation. This method was utilized to predict the structure of ^{17}O [3, 4] and successfully yielded solutions for bound levels as well as for the low-lying $1d_{3/2}$ resonance. Specifically, for the $1d_{3/2}$ level, the energy (width) of the level was predicted to be $\sim$ 1 MeV ($\sim$ 100 keV), which agrees well with the

This research was partially supported by the National Natural Science Foundation of China (Nos. 12175010, 11375022, 11775014), Strategic Priority Research Program of the Chinese Academy of Sciences (No. XDB34010000), and US Department of Energy Office of Science, Office of Nuclear Physics, under Award Number DE-AC05-00OR22725.

✉ Shi-Sheng Zhang
zss76@buaa.edu.cn

Michael Scott Smith
smithms@ornl.gov

[1] School of Physics, Beihang University, Beijing 100191, China

[2] Physics Division, Oak Ridge National Laboratory, Oak Ridge, TN 37831-6354, USA

experimental value [5] of 0.944 MeV (88 keV). However, the RAB approach was unable to obtain a solution for the critical $2p_{3/2}$ orbital, making it necessary to consider the experimental values for this level in the studies of $^{16}O(n,\gamma)^{17}O$ reaction in Refs. [3, 4].

It is quite difficult to achieve a structure of low-lying excited states with negative parity, which was also proposed in the shell model [6] combined with the complex scaling method (CSM) [7, 8]. The CSM is applicable to resonances with a small rotation angle θ, but it is difficult to detect those with larger rotation angles, such as the $2p_{3/2}$ level in ^{31}Ne [8]. Another approach, based on a complex momentum representation (CMR) of the Schrödinger equation, sought to overcome the limitations of the CSM approach and describe both the bound and resonant levels in ^{17}O but failed to obtained a solution for the critical low-lying $2p_{3/2}$ level in Ref. [9]. As described below, this study utilizes the CMR approach but is based on a new nuclear potential improving the result reported in Ref. [3] for ^{17}O to predict the structure of the important $2p_{3/2}$ resonance.

Near-threshold resonances with low angular momentum are not just important for astrophysical capture reactions. A number of studies have demonstrated that such resonances can be critical in the formation of halo structures in some exotic nuclei [10–12]. The study of halo nuclei and related exotic nuclear structure phenomena [13–17] are the main motivations for novel unstable beam facilities (*e.g.*, FRIB [18], FAIR [19]). Moreover, understanding the exotic nuclear structure has been identified as a top priority for theoretical research communities (*e.g.*, FRIB [20]). It is important to advance our understanding of the resonances that may drive the formation of nuclear halos.

Numerous studies have focused on the possible halos in neutron-rich fluorine isotopes, especially for $^{29,31}F$. These studies have been driven by the importance of understanding the extent of the "island of inversion" as well as shell evolution across the fluorine isotopic chain [21]. Experimental studies have been conducted on halo structures [22–26] and theoretical studies [21, 27]. Bagchi *et al.* [22] demonstrated the presence of a two-neutron Borromean halo in the ground state of ^{29}F, which was thought to be dominated by the p-orbital. Subsequently, a scattering phase-shift method was used in a theoretical study of the bound and resonant orbitals in ^{29}F [28]. This study utilized both spherical and deformed Woods–Saxon potentials and found solutions for three bound levels ($1d_{3/2}$, $2s_{1/2}$, and $1d_{5/2}$) and one resonant orbital ($1f_{7/2}$).

However, there are hints in our calculations based on a deformed relativistic Hartree–Bogoliubov theory in continuum (DRHBc) theory [29] that ^{29}F is spherical with deformation $\beta \simeq 0$. In the spherical calculation stated in Ref. [28], however, a solution could not be found for the single-particle $2p_{3/2}$ resonant level. Because of the possible role this level could play in forming the ^{29}F or ^{31}F halo, it is critical to understand the properties of this resonant level.

In this study, our CMR methodology is described in Sect. 2, whereas the results for the critical $2p_{3/2}$ and $1d_{3/2}$ resonances in ^{17}O are presented in Sect. 3. The latter section details the results of CMR predictions regarding the energies of the low-lying $2p_{3/2}$ resonant orbitals in $^{29,31}F$, which affect the formation mechanism of a halo. Finally, a summary is given in Sect. 4.

2 Methods

To describe the methodology of this study, theoretical details of the CMR framework, nuclear potential, integration approach, and convergence and accuracy of the integration are presented in this section. Throughout this section, we use the example of the low-lying resonant orbitals of ^{17}O to demonstrate the viability of this approach.

2.1 Formalism

In this section, a unified description of the bound and unbound states described by the CMR method is given based on the spherical case, similar to the description presented in Ref. [9]. A more general formalism can be found in Ref. [30]. A Hamiltonian of the form

$$\hat{H} = \hat{T} + \hat{V}, \tag{1}$$

is assumed, where $\hat{T}$ is the kinetic energy and $\hat{V}$ is the nuclear potential with a Woods–Saxon shape. The foundation of the CMR approach [9] describes the Schrödinger equation with this Hamiltonian in momentum, rather than coordinate, is represented as:

$$\int d^3\vec{k}' \left\langle \vec{k} \middle| \hat{H} \middle| \vec{k}' \right\rangle \Phi_n(\vec{k}') = E_n \Phi_n(\vec{k}). \tag{2}$$

Here, $\vec{k} = \vec{p}/\hbar$ is the wave vector, $\Phi_n(\vec{k})$ is the wave function, and E_n is the energy of the nth state. If we assume spherical symmetry, the wave function can be stated as follows:

$$\Phi_n(\vec{k}) = \phi_n(k) Y_l^m(\Omega_k), \tag{3}$$

where $\phi_n(k)$ is the radial portion of the momentum wavefunction and $Y_l^m(\Omega_k)$ is the angular portion with angular momentum quantum numbers l and m. The Schrodinger equation then becomes:

$$\frac{\hbar^2 k^2}{2m} \phi_n(k) + \int dk' k'^2 V_l(k,k') \phi_n(k') = E_n \phi_n(k), \tag{4}$$

with

$$V_l(k,k') = \frac{2}{\pi}\int drr^2 V(r) j_l(kr) j_l(k'r), \tag{5}$$

where $j_l(kr)$ denotes the spherical Bessel function of lth order. Equation (5) is the integral of the potential given in Sect. (2.2) in a Woods–Saxon formulation over the coordinate space. Subsequently, this expression is used in Eq. (4) in an integral of the product of the potential and wavefunction over the momentum space in the CMR-based Schrödinger equation. The solution of these equations for eigenvalue level energies E_n is discussed in Sect. (2.3).

2.2 Potential parameters

In Ref. [9], the CMR method was used to calculate the low-lying resonances in ^{17}O with a generic Woods–Saxon potential described in Ref. [31]. Because this potential does not reproduce the experimental one-neutron separation energy, the predicted energy and width of the resonant orbital $1d_{3/2}$ are significantly overestimated. More importantly, a CMR-based solution for the energy level of the low-lying resonant $2p_{3/2}$ orbital, whose contributions become progressively important and comparable to the direct capture process above 70 keV [3, 4], cannot be found in that research.

Therefore, we adopted the potential based on that presented in Ref. [3] to revisit the bound and resonant structures in ^{17}O. The interaction potential V includes the central part V_C and spin-orbit part V_{SO}, which takes the form of the Woods–Saxon-type potential,

$$V_C(r) = V_0 f_C(r), \tag{6}$$

$$V_{SO}(r) = -V_{SO}^0\left(\frac{\hbar}{m_\pi c}\right)^2 (\vec{l}\cdot\vec{s})\frac{1}{r}\frac{df_{SO}(r)}{dr}, \tag{7}$$

$$f_i(r) = \frac{1}{1+\exp((r-R_i)/a_i)}, \quad (i \text{ refers to C or SO}). \tag{8}$$

Here, the pion Compton wavelength $\hbar/m_\pi c = 1.414$ fm and potential depth V_0 for the central part and V_{SO}^0 for the spin-orbit part were adjusted to reproduce the one-neutron separation energy $S_n = 4.143$ MeV for ^{17}O. The diffuseness and radius parameters are obtained from the Koning-Delaroche optical model potential [32]. The six parameters of the Woods–Saxon potential are listed in Table 1.

In the case of exotic neutron-rich fluorine isotopes ^{29,31}F, a standard spherical potential [31] was adopted, which was also utilized in a recent study focusing on this nucleus using a scattering phase shift method [28]. By choosing this potential, a direct comparison can be made between the CMR method and scattering phase-shift approach.

Table 1 Adopted parameters in Woods–Saxon potential for ^{17}O

Parameter	Adopted value
V_0 (MeV)	−58.75
V_{SO}^0 (MeV)	−12.45
a_0 (fm)	0.675
a_{SO} (fm)	0.590
r_0 (fm)	2.947
r_{SO} (fm)	2.401

2.3 Integration method

The integral stated in Eq. (4) requires discretization to readily obtain the eigenvalue level energies E_n. The integral over the momentum space can be approximated as a sum over a finite N_q set of points k_j with spacing dk and weights w_j. The result is the following $N_q \times N_q$ matrix equation:

$$\sum_{j=1}^{N_q} H_{i,j}\phi_n(k_j) = E_n\phi_n(k_i), \quad (i = 1,2,\cdots,N_q), \tag{9}$$

$$H_{i,j} = \frac{\hbar^2 k_i^2}{2m}\delta_{i,j} + w_j k_j^2 V_l^{i,j}, \tag{10}$$

$$V_l^{i,j} = \frac{2}{\pi}\int drr^2 V(r) j_l(k_i r) j_l(k_j r). \tag{11}$$

Using the following transformations:

$$\phi_n'(k_i) = \sqrt{w_i}k_i\phi_n(k_i), \quad H_{i,j}' = \sqrt{\frac{w_i}{w_j}}\frac{k_i}{k_j}H_{i,j}, \tag{12}$$

the system for the n^{th} state is symmetrized as follows:

$$\sum_{j=1}^{N_q} H_{i,j}'\phi_n'(k_j) = E_n\phi_n'(k_i), \quad (i = 1,2,\cdots,N_q), \tag{13}$$

$$H_{i,j}' = \frac{\hbar^2 k_i^2}{2m}\delta_{i,j} + \sqrt{w_i w_j}k_i k_j V_l^{i,j}, \tag{14}$$

$$V_l^{i,j} = \frac{2}{\pi}\int drr^2 V(r) j_l(k_i r) j_l(k_j r). \tag{15}$$

where $k_{i,j}$ denote the integral points along a contour in the momentum space with corresponding weights $w_{i,j}$; the potential is integrated over the coordinate space. It is known (see, *e.g.*, Refs. [33–35]) that bound states populate the imaginary axis in the momentum plane, whereas resonances are located within the fourth quadrant. By choosing the grid points $k_{i,j}$ along an appropriate path in the *complex* momentum plane that contains these levels, the eigenvalues—single particle energies—of this system for the bound, resonant, and continuum states can be determined.

Because the integration stated in Eq. (4) ranges from zero to infinity, the sum stated in Eq. (13) must be carried out up to large momentum values. Therefore, we adopt a Gauss–Legendre quadrature approach to obtain solutions for the eigenenergies E_n. Similarly, we apply the Gauss–Legendre quadrature to the coordinate-space integral stated in Eq. (15). In Ref. [9], a Gauss–Legendre quadrature method was used for the momentum integral, while a Gauss–Hermite quadrature method was used for the coordinate (potential) integral; the resulting accuracy for single-particle energies was 10^{-4} MeV. The selection of the number of grid points and truncation in the momentum and coordinate space will influence the convergence of the summation (integration) for both the momentum and coordinate integrals, as well as the value and precision of the single-particle energy level solutions. The convergence and accuracy characteristics are provided in the next subsection.

2.4 Convergence and accuracy

In coordinate space, we study the convergence and accuracy of the potential integral $V_{i,j}$ presented in Eq. (15) with variations in the number of grid points N_p and truncation (maximum value) of the radius $r_{\rm cut}$ in the integral. Integral accuracy is defined as the maximum accuracy for the real and imaginary parts of the integral. For a particular choice of momentum values $k_i = (0.3, -0.075)$ and $k_j = (0.4, 0)$, where the units of the real and imaginary components of the momentum grid points are given in fm^{-1}, Fig. 1 demonstrates the smooth convergence of the coordinate-space potential integral. Moreover, an accuracy of 10^{-10} MeV, which is well-beyond the required precision of the calculation, can be reached when $N_p \geq 90$ and $r_{\rm cut} \geq 30$ fm. To guarantee convergence with this accuracy, we utilize $N_p = 100$ and $r_{\rm cut} = 40$ fm in our subsequent coordinate-space potential integral calculations.

Similarly, in the momentum space, we study the convergence of the solutions to the system of equations presented in Eqs. (13) and (14) with variations in the number of grid points N_q and truncation (maximum value) of the momentum $k_{\rm cut}$ in the integral. The path for momentum integration is selected as a contour bounded by points (0, 0), (0.5, −0.1), (1, 0) and (10, 0) in the complex momentum plane. For each segment of the contour, the number of grid points for the Gauss–Legendre quadrature is N_q, such that the total number of grid points for the entire path is $3N_q$. The positions of the complex momentum for the resonant states do not change with the different paths of the contour.

Figure 2 demonstrates an example of the convergence of the momentum-space integral for the $1d_{3/2}$ resonant orbital in ^{17}O. An accuracy of 10^{-8} MeV can be achieved when $N_q \geq 40$ and $k_{\rm cut} \geq 7.5$ fm^{-1}. To guarantee convergence with such accuracy, we utilize $N_q = 100$ and $k_{\rm cut} = 10$ fm^{-1} in our solution of the momentum-space integral. For this level, the converged values are 1.038 MeV and 0.149 MeV for the energy and width, respectively, which are consistent with the measured values of 0.944 ± 0.001 MeV and 0.088 ± 0.003 MeV [5].

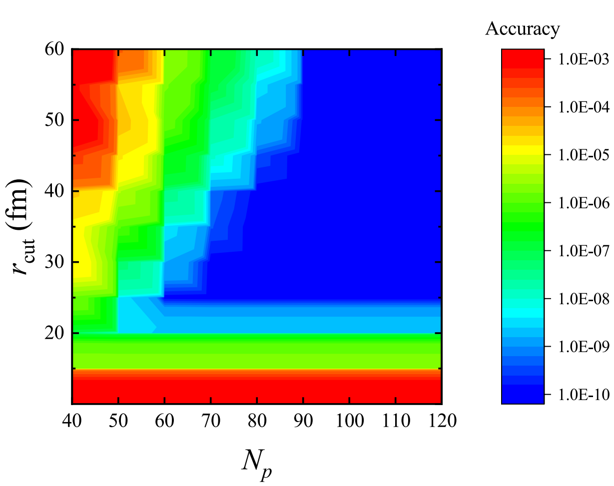

Fig. 1 (Color online) Accuracy variation in the coordinate-space potential integrals $V_{i,j}$ (in MeV) with the number of grid points N_p and cut-off radius $r_{\rm cut}$ at $k_i = (0.3, -0.075)$, $k_j = (0.4, 0)$

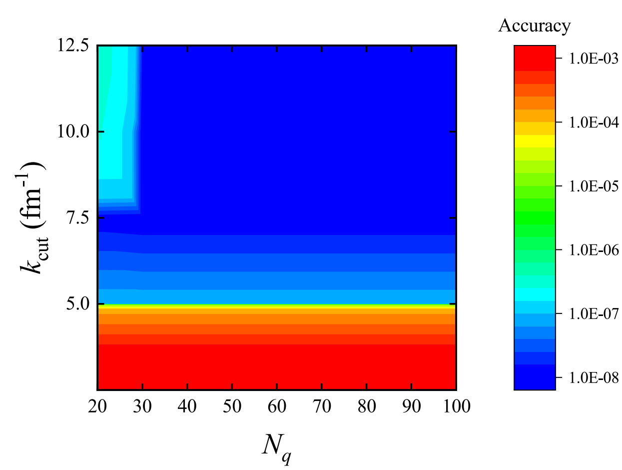

Fig. 2 (Color online) Accuracy variation in the energy and decay width (in MeV) for the $1d_{3/2}$ single particle state in ^{17}O with the momentum-space number of grid points N_q and cut-off of wave vector $k_{\rm cut}$

3 Results and discussions

3.1 Energy levels for bound and resonant states in ^{17}O

The CMR approach described above was used to solve for the bound and resonant states in ^{17}O. The contour for the momentum integration, as shown in Fig. 3, is bounded by points (0, 0), (0.25, −0.5), (0.5, 0), and (10, 0) in the complex momentum plane. This contour was chosen to include the ^{17}O bound states (indicated with the blue open squares in Fig. 3) on the positive imaginary k axis, resonant states (indicated with the red open triangles) confined and scattered inside the contour, and continuum states (indicated with the black open circles) distributed along the contour. The positions of the bound and resonant states remained unchanged with different contour shapes.

The CMR-based solutions for the five bound states and two resonant states of ^{17}O are listed in Table 2. Experimental data from Refs. [5, 36–38] are presented for comparison. Additionally, the Numerov numerical method (see, *e.g.*, Ref. [39]) can be used to solve the Schrödinger equation for negative-energy (bound) levels to an arbitrary level of precision, including a Woods–Saxon potential formulation (see, *e.g.*, Ref. [40]). The results of the Numerov approach for the five bound ^{17}O levels using the potential described in Sect. 2.2 are reported in Table 2, underlining that the CMR results agree with the Numerov approach within 0.001 MeV. The CMR results agree with the experimental value of the $2s_{1/2}$ excited state energy within 0.1 MeV.

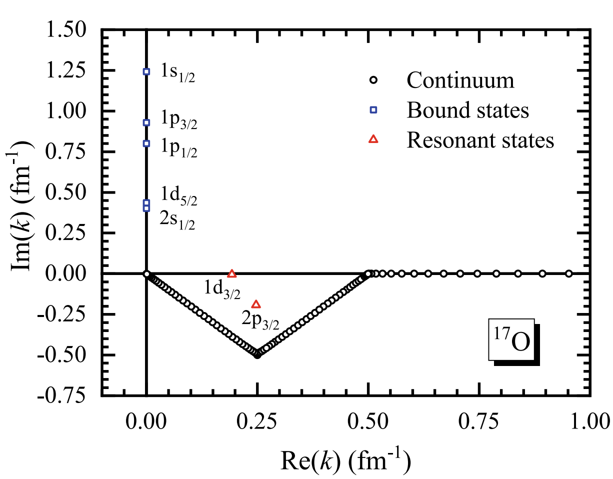

Fig. 3 Single neutron spectra for ^{17}O in complex momentum plane. The blue open squares, red open triangles, and black open circles represent the bound states, resonant states, and continuum states, respectively. The momentum integration contour is defined by the points (0, 0), (0.25, −0.5), (0.5, 0), and (10, 0)

Table 2 Predictions for the five bound states, and two resonant states (labeled in bold), of ^{17}O via the CMR method and Numerov method. The experimental data are also shown for comparison and taken from Refs. [5, 36–38]. Energies E and decay widths Γ are in the unit of MeV

	This work		Numerov	Experiment	
	E	Γ	E	E	Γ
$1s_{1/2}$	−33.985		−33.985		
$1p_{3/2}$	−18.992		−18.992		
$1p_{1/2}$	−13.872		−13.872		
$1d_{5/2}$	−4.143		−4.143	−4.143 [a]	
$2s_{1/2}$	−3.381		−3.381	−3.272 [b]	
$2p_{3/2}$	0.498	4.417		0.411 [c]	0.040 [c]
$1d_{3/2}$	1.038	0.149		0.944 [d]	0.088 [d]

[a] Reference [36]
[b] Reference [37]
[c] Reference [38]
[d] Reference [5]

For the $1d_{3/2}$ resonant orbital, the CMR approach provides a solution at position (0.217, −0.008) in the complex momentum plane, corresponding to a resonance energy $E_R = 1.038$ MeV and decay width $\Gamma = 0.149$ MeV. The energy is within 10% of the measured value of $E_R^{\text{Exp}} = 0.944 \pm 0.001$ MeV [5]; the width is within 0.06 MeV of the measured value of $\Gamma^{\text{Exp}} = 0.088 \pm 0.003$ MeV [5].

For the critical $2p_{3/2}$ low-lying resonant orbital, the solutions for which have not been obtained with previous theoretical approaches, the CMR approach using the potential stated in Sect. 2.2 yields a predicted energy of 0.498 MeV, which is within 22% of the measured value of $E_R^{\text{Exp}} = 0.411$ MeV [38]. This result demonstrates the potential of the CMR method for predicting low-lying odd-parity levels. However, the CMR-based prediction of the width of this critical level is 4.417 MeV, which is much larger than the experimental value of 0.040 MeV. This overestimation of the low-lying resonance width has appeared in other CMR-based studies (see, *e.g.*, Refs. [9, 41]). The measured $3/2^-$ orbital may originate from ^{16}O core excitation [6, 42], which should be treated beyond the mean-field framework. In Ref. [42], the Shell Model Embedded in the Continuum (SMEC) was used to study the spectroscopy of mirror nuclei: ^{17}O and ^{17}F, where realistic SM solutions for (quasi-) bound states were coupled to the one-particle scattering continuum for both Wigner and Bartlett (WB) and density-dependent (DDSM1) residual interactions. All these SMEC predictions of the level energies with residual interactions for $3/2^-$ state in ^{17}O are approximately 0.5 MeV larger than the experimental data with widths of 40 keV. As mentioned in Ref. [6], the potential model does not include particle-hole excitation in

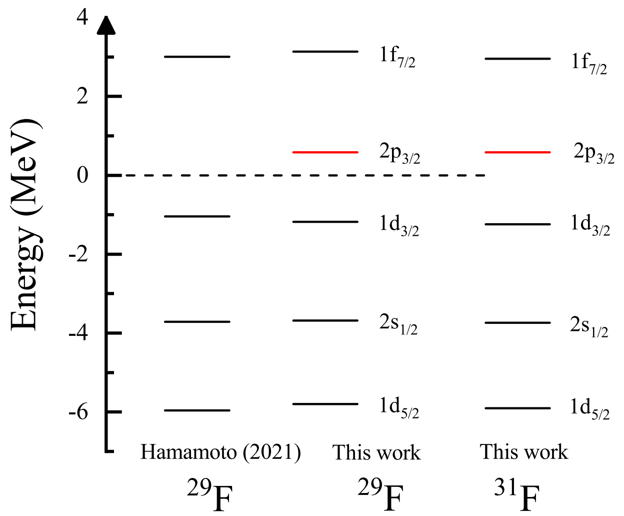

Fig. 4 Levels in ^{29}F and ^{31}F around the threshold with spherical assumption. Levels on the left for ^{29}F are taken from Ref. [28]. Our predictions are shown on the right, in which orbitals $2p_{3/2}$ are plotted in red

the ^{16}O core in their calculations; thus, low-lying negative-parity states, such as $3/2^-$, cannot be reproduced. Therefore, our evaluation of the width might be narrower when the core excitation is considered.

3.2 Energy levels for bound and resonant states in ^{29}F and ^{31}F

The exotic nuclei ^{29}F and ^{31}F, which are candidates for a two-neutron Borromean halo structure [22], were studied using the same CMR approach as that used for ^{17}O. As the separation energy has not been measured in this nucleus, a standard set [31] of potential parameters is used for ^{29,31}F, which is the same as that used in Ref. [28]. The integration contour in the complex momentum space is bounded by points $(0,\ 0)$, $(0.25,\ -0.5)$, $(0.5,\ 0)$ and $(10,\ 0)$.

The results for the bound and resonant states in ^{29}F and ^{31}F, respectively, are shown in Fig. 4. Owing to the lack of experimental measurements regarding the excited states of this nucleus, a comparison is made in Fig. 4 between our CMR-based predictions and those obtained using the scattering phase-shift method described in Ref. [28]. The energies for the bound orbitals and unbound $1f_{7/2}$ orbital in ^{29}F agree well with those stated in Ref. [28] with a maximum difference of 0.15 MeV. Most importantly, our prediction of the critical low-lying negative-parity $2p_{3/2}$ resonant orbital in ^{29}F is only 0.582 MeV above the neutron threshold; a solution for this level is not presented in Ref. [28]. In the spherical case of ^{29}F, the predicted $2p_{3/2}$ lies above $1d_{3/2}$, which is consistent with conditions B and C described in Ref. [21]. From the calculated spectrum in ^{31}F, we can determine that the last two neutrons occupy $2p_{3/2}$, which might cause the halo formation in ^{31}F. As was the case for predicting the width of the $2p_{3/2}$ resonance orbital in ^{17}O. The prediction of the decay width of the $2p_{3/2}$ orbital in ^{29}F (^{30}F)—2.384 MeV (2.337 MeV)—is likely significantly overestimated by the CMR approach and warrants further study. If deformation is considered, the $2p_{3/2}$ orbital might be lower than the $1d_{3/2}$ orbital, which will be studied in our future research.

4 Summary

Solving the Schrödinger equation in a complex momentum space, rather than coordinate space, enables the bound and resonant levels to be treated simultaneously in a uniform manner. The viability of this approach for predicting the energies of low-lying resonances above the particle threshold has been explored focusing on the critical levels in ^{17}O and ^{29,31}F. Using a novel nuclear potential based on Koning-Delaroche optical model potential constrained by the experimental one-neutron separation energy. Subsequently, the energy of the low-lying resonant $2p_{3/2}$ orbital in ^{17}O is determined as 0.498 MeV in agreement with the experimental results. The predicted energy and width of the $1d_{3/2}$ level agree well with the measured data as well. These two levels are known to dominate neutron capture on ^{16}O which acts as a neutron poison in weak s-process nucleosynthesis. In addition, the CMR approach was utilized to examine the levels in ^{29}F and ^{31}F exotic nuclei with two possible neutron halo structures. The CMR approach predicts the energies of the bound levels and unbound $1f_{7/2}$ level in ^{29}F, which agree well with the results of the phase-shift method. Most importantly, the CMR approach predicts that the $2p_{3/2}$ orbital lies just above the threshold, which is critical for halo formation in ^{31}F. These results demonstrate that when coupled with the proper nuclear potential, the CMR approach is a promising tool for determining resonance energies, especially for low-lying orbitals with negative parity that are crucial in capture reactions and halo formation. In the future, we will improve the overestimated decay widths with a dedicated formalism [43], wherein occupation probabilities can be estimated by BCS approximation with particle-hole residual interactions for core excitation.

Acknowledgements The authors would like to express their gratitude for the valuable discussions with Jian-You Guo.

Author Contributions All authors contributed to the study conception and design. Material preparation, data collection and analysis were performed by Si-Zhe Xu, Shi-Sheng Zhang, Xiao-Qian Jiang, and Michael Scott Smith. The first draft of the manuscript was written by Si-Zhe Xu, Shi-Sheng Zhang, and Michael Scott Smith, and all authors commented on previous versions of the manuscript. All authors read and approved the final manuscript.

References

1. N. Prantzos, M. Hashimoto, K. Nomoto, The s-process in massive stars-yields as a function of stellar mass and metallicity. Astron. Astrophys. **234**, 211–229 (1990).
2. P. Mohr, C. Heinz, M. Pignatari et al., Re-evaluation of the ^{16}O$(n,\gamma)^{17}$O cross section at astrophysical energies and its role as a neutron poison in the s-process. Astrophys. J. **827**, 29 (2016). https://doi.org/10.3847/0004-637x/827/1/29
3. M. He, S.-S. Zhang, M. Kusakabe et al., Nuclear structures of ^{17}O and time-dependent sensitivity of the weak s-process to the ^{16}O$(n,\gamma)^{17}$O rate. Astrophys. J. **899**, 133 (2020). https://doi.org/10.3847/1538-4357/aba7b4
4. S. Zhang, S. Xu, M. He et al., Neutron capture on ^{16}O within the framework of rmf+ accc+ bcs for astrophysical simulations. Eur. Phys. J. A **57**, 1–7 (2021). https://doi.org/10.1140/epja/s10050-021-00434-7
5. T. Faestermann, P. Mohr, R. Hertenberger et al., Broad levels in ^{17}O and their relevance for the astrophysical *s* process. Phys. Rev. C **92**, 052802 (2015). https://doi.org/10.1103/PhysRevC.92.052802
6. K. Yamamoto, H. Masui, K. Katō et al., Radiative Capture Cross Section for ^{16}O$(n,\gamma)^{17}$O and ^{16}O$(p,\gamma)^{17}$ F below Astrophysical Energies. Prog. Theor. Phys. **121**, 375–390 (2009). https://doi.org/10.1143/PTP.121.375
7. N. Michel, W. Nazarewicz, M. Płoszajczak et al., Shell model in the complex energy plane. J. Phys. G **36**, 013101 (2008). https://doi.org/10.1088/0954-3899/36/1/013101
8. Q. Liu, J.-Y. Guo, Z.-M. Niu et al., Resonant states of deformed nuclei in the complex scaling method. Phys. Rev. C **86**, 054312 (2012). https://doi.org/10.1103/PhysRevC.86.054312
9. Y.-J. Tian, T.-H. Heng, Z.-M. Niu et al., Exploration of resonances by using complex momentum representation. Chin. Phys. C **41**, 044104 (2017). https://doi.org/10.1088/1674-1137/41/4/044104
10. S.-G. Zhou, J. Meng, P. Ring et al., Neutron halo in deformed nuclei. Phys. Rev. C **82**, 011301 (2010). https://doi.org/10.1103/PhysRevC.82.011301
11. A. Moro, J. Lay, Interplay between valence and core excitation mechanisms in the breakup of halo nuclei. Phys. Rev. Lett. **109**, 232502 (2012). https://doi.org/10.1103/PhysRevLett.109.232502
12. S.-S. Zhang, M.S. Smith, Z.-S. Kang et al., Microscopic self-consistent study of neon halos with resonant contributions. Phys. Lett. B **730**, 30–35 (2014). https://doi.org/10.1016/j.physletb.2014.01.023
13. L. Zhou, S.M. Wang, D.Q. Fang, Y.G. Ma, Recent progress in two-proton radioactivity. Nucl. Sci. Tech. **33**, 105 (2022). https://doi.org/10.1007/s41365-022-01091-1
14. B. Li, N. Tang, Y.H. Zhang et al., Production of p-rich nuclei with Z=20-25 based on radioactive ion beams. Nucl. Sci. Tech. **33**, 55 (2022). https://doi.org/10.1007/s41365-022-01048-4
15. D.S. Ahn, N. Fukuda, H. Geissel et al., Location of the neutron dripline at fluorine and neon. Phys. Rev. Lett. **123**, 212501 (2019). https://doi.org/10.1103/PhysRevLett.123.212501
16. W. Nan, B. Guo, C.J. Lin et al., First proof-of-principle experiment with the post-accelerated isotope separator on-line beam at BRIF: measurement of the angular distribution of ^{23}Na + ^{40}Ca elastic scattering. Nucl. Sci. Tech. **32**, 53 (2021). https://doi.org/10.1007/s41365-021-00889-9
17. S.W. Bai, X.F. Yang, S.J. Wang et al., Commissioning of a high-resolution collinear laser spectroscopy apparatus with a laser ablation ion source. Nucl. Sci. Tech. **33**, 9 (2022). https://doi.org/10.1007/s41365-022-00992-5
18. B. M. Sherrill, Future opportunities at the facility for rare isotope beams, in:EPJ Web of Conferences, vol. 178, EDP Sciences, 2018, p. 01001. https://doi.org/10.1051/epjconf/201817801001
19. T. Nilsson, Radioactive ion beams at fair-nustar. Eur. Phys. J-Spec. Top. **156**, 1–12 (2008). https://doi.org/10.1140/epjst/e2008-00606-2
20. A. Balantekin, J. Carlson, D. Dean et al., Nuclear theory and science of the facility for rare isotope beams. Mod. Phys. Lett. A **29**, 1430010 (2014). https://doi.org/10.1142/S0217732314300109
21. J. Singh, J. Casal, W. Horiuchi et al., Exploring two-neutron halo formation in the ground state of ^{29}F within a three-body model. Phys. Rev. C **101**, 024310 (2020). https://doi.org/10.1103/PhysRevC.101.024310
22. S. Bagchi, R. Kanungo, Y.K. Tanaka et al., Two-neutron halo is unveiled in ^{29}F. Phys. Rev. Lett. **124**, 222504 (2020). https://doi.org/10.1103/PhysRevLett.124.222504
23. A. Revel, O. Sorlin, F.M. Marqués, SAMURAI21 collaboration et al., Extending the southern shore of the island of inversion to ^{28}F. Phys. Rev. Lett. **124**, 152502 (2020). https://doi.org/10.1103/PhysRevLett.124.152502
24. D.Z. Chen, D.L. Fang, C.L. Bai, Impact of finite-range tensor terms in the Gogny force on the β-decay of magic nuclei. Nucl. Sci. Tech. **32**, 74 (2021). https://doi.org/10.1007/s41365-021-00908-9
25. G. Christian, N. Frank, S. Ash et al., Exploring the low-*z* shore of the island of inversion at $n = 19$. Phys. Rev. Lett. **108**, 032501 (2012). https://doi.org/10.1103/PhysRevLett.108.032501
26. L. Gaudefroy, W. Mittig, N. Orr et al., Direct mass measurements of ^{19}B, ^{22}C, ^{29}F, ^{31}Ne, ^{34}Na and other light exotic nuclei. Phys. Rev. Lett. **109**, 202503 (2012). https://doi.org/10.1103/PhysRevLett.109.202503
27. H. Masui, W. Horiuchi, M. Kimura, Two-neutron halo structure of f 31 and a novel pairing antihalo effect. Phys. Rev. C **101**, 041303 (2020). https://doi.org/10.1103/PhysRevC.101.041303
28. I. Hamamoto, Deformed halo of 29F. Phys. Lett. B **814**, 136116 (2021). https://doi.org/10.1016/j.physletb.2021.136116
29. L. Li, J. Meng, P. Ring et al., Deformed relativistic hartree-bogoliubov theory in continuum. Phys. Rev. C **85**, 024312 (2012). https://doi.org/10.1103/PhysRevC.85.024312
30. G. Hagen, J.S. Vaagen, Study of resonant structures in a deformed mean field by the contour deformation method in momentum space. Phys. Rev. C **73**, 034321 (2006). https://doi.org/10.1103/PhysRevC.73.034321
31. A. Bohr, B.R. Mottelson, *Nuclear Structure*, vol. I (World Scientific, Singapore, 1998)
32. A. Koning, J. Delaroche, Local and global nucleon optical models from 1 keV to 200 MeV. Nucl. Phys. A **713**, 231–310 (2003). https://doi.org/10.1016/S0375-9474(02)01321-0
33. C.V. Sukumar, Schrodinger equation in momentum space. J. Phys. A Mathematic. General **12**, 1715–1730 (1979). https://doi.org/10.1088/0305-4470/12/10/018
34. Y.R. Kwon, F. Tabakin, Hadronic atoms in momentum space. Phys. Rev. C **18**, 932–943 (1978). https://doi.org/10.1103/PhysRevC.18.932
35. N. Li, M. Shi, J.-Y. Guo et al., Probing resonances of the dirac equation with complex momentum representation. Phys. Rev. Lett. **117**, 062502 (2016). https://doi.org/10.1103/PhysRevLett.117.062502
36. M. Wang, W. Huang, F. Kondev et al., The AME 2020 atomic mass evaluation (II). Tables, graphs and references. Chin. Phys. C **45**, 030003 (2021). https://doi.org/10.1088/1674-1137/abddaf
37. R.B. Firestone, Z. Revay, Thermal neutron capture cross sections for ^{16,17,18}O and ^{2}H. Phys. Rev. C **93**, 044311 (2016). https://doi.org/10.1103/PhysRevC.93.044311

38. Y. Nagai, M. Kinoshita, M. Igashira et al., Nonresonant *p*-wave direct capture and interference effect observed in the ^{16}O $(n, \gamma)^{17}O$ reaction. Phys. Rev. C **102**, 044616 (2020). https://doi.org/10.1103/PhysRevC.102.044616
39. M. Pillai, J. Goglio, T.G. Walker, Matrix numerov method for solving schrödinger equation. Am. J. Phys. **80**, 1017–1019 (2012). https://doi.org/10.1119/1.4748813
40. M. Bhat, A.P. Monteiro, in *Numerical solution of schroedinger equation using matrix numerov method with woods - saxon potential*. Proceedings of the DAE-BRNS symposium on nuclear physics, Prasanthi Nilayam (India), 2015, pp.7–11
41. Y.-X. Luo, K. Fossez, Q. Liu et al., Role of quadrupole deformation and continuum effects in the "island of inversion" nuclei $^{28,29,31}F$. Phys. Rev. C **104**, 014307 (2021). https://doi.org/10.1103/PhysRevC.104.014307
42. K. Bennaceur, F. Nowacki, J. Okołowicz et al., Analysis of the ^{16}O (p, γ) ^{17}F capture reaction using the shell model embedded in the continuum. Nucl. Phys. A **671**, 203–232 (2000). https://doi.org/10.1016/S0375-9474(99)00851-9
43. G. Cattapan, E. Maglione, From bound states to resonances: analytic continuation of the wave function. Phys. Rev. C **61**, 067301 (2000). https://doi.org/10.1103/PhysRevC.61.067301